

H α AND 4000 Å BREAK MEASUREMENTS FOR \sim 3500 *K*-SELECTED GALAXIES AT $0.5 < z < 2.0$

MARISKA KRIEK¹, PIETER G. VAN DOKKUM², KATHERINE E. WHITAKER², IVO LABBÉ³, MARIJN FRANX³, & GABRIEL B. BRAMMER⁴

Accepted for publication in ApJ

ABSTRACT

We measure spectral features of \sim 3500 *K*-selected galaxies at $0.5 < z < 2.0$ from high quality medium-band photometry using a new technique. First, we divide the galaxy sample in 32 subsamples based on the similarities between the full spectral energy distributions (SEDs) of the galaxies. For each of these 32 galaxy types we construct a composite SED by de-redshifting and scaling the observed photometry. This approach increases the signal-to-noise ratio and sampling of galaxy SEDs and allows for model-independent stellar population studies. The composite SEDs are of spectroscopic quality, and facilitate – for the first time – H α measurement for a large magnitude-limited sample of distant galaxies. The linewidths indicate a photometric redshift uncertainty of $\Delta z < 0.02 \times (1 + z)$. The composite SEDs also show the Balmer and 4000 Å breaks, Mg II absorption at \sim 2800 Å, the dust absorption feature at 2175 Å, and blended [O III]+H β emission. We compare the total equivalent width of H α , [N II], and [S II] ($W_{\text{H}\alpha+}$) with the strength of the 4000 Å break ($D(4000)$) and the best-fit specific star formation rate, and find that all these properties are strongly correlated. This is a reassuring result, as currently most distant stellar population studies are based on just continuum emission. Furthermore, the relation between $W_{\text{H}\alpha+}$ and $D(4000)$ provides interesting clues to the SFHs of galaxies, as these features are sensitive to different stellar ages. We find that the correlation between $W_{\text{H}\alpha+}$ and $D(4000)$ at $0.5 < z < 2.0$ is similar to $z \sim 0$, and that the suppression of star formation in galaxies at $z < 2$ is generally not abrupt, but a gradual process.

Subject headings: galaxies: evolution — galaxies: stellar content

1. INTRODUCTION

Galaxies in the local universe give us many clues to their star formation histories (SFHs). Massive elliptical galaxies can have stellar ages nearly as old as the age of the universe, while spiral galaxies are still forming new stars. Detailed studies of nearby stellar populations allow accurate age measurements, and thus a measure of the SFHs in these systems. While such detailed studies will never be possible at cosmological distances, studying galaxies throughout cosmic time offers another advantage: we can directly study their masses and star formation rates (SFRs) at different phases in their lives, rather than inferring these quantities from age measurements.

In the past few years, photometric and spectroscopic galaxy surveys have started to explore the universe at redshifts $z = 1 - 3$, the peak of the quasar era and the epoch when the volume-averaged SFR of the Universe was at its maximum (e.g., Bouwens et al. 2011). This peak is at least in part caused by a population of galaxies with apparently very high specific SFR (SSFR; SFR divided by stellar mass) (e.g., Noeske et al. 2007a,b; Davis et al. 2007; Salim et al. 2007; Elbaz et al. 2007; Damen et al. 2009; Oliver et al. 2010; Papovich et al. 2011). Remarkably, at the same time there are galaxies that appear to have already

stopped forming stars. Massive, quiescent galaxies have been identified out to at least $z \sim 2.5$ (e.g., McCarthy et al. 2004; Labbé et al. 2005; Kriek et al. 2006b, 2008b; Cimatti et al. 2008; Williams et al. 2009; Brammer et al. 2009; Whitaker et al. 2010), implying that they formed their stars at even earlier times.

A major complication in all high-redshift studies is the lack of uniform and reliable measurements of SFHs. In the local universe, the “standard” indicator of the instantaneous SFR is the H α emission line (e.g., Kennicutt 1998) and a standard indicator of the age of a stellar population is the strength of the 4000 Å HK continuum break (e.g., Kauffmann et al. 2003a). At redshifts $z > 1$, both features shift into the observed near-infrared (NIR) and are very difficult to measure. As a result, studies of galaxies at $z > 1$ are either limited to small and often biased samples (e.g., Erb et al. 2006a,b,c; Kriek et al. 2006a, 2007, 2008a; Muzzin et al. 2009, 2010; Reddy et al. 2010) or are based on SFH indicators that are less robust and less well calibrated, such as broadband spectral energy distributions (SEDs) (e.g., van Dokkum et al. 2006; Labbé et al. 2007; Papovich et al. 2007, 2011; Damen et al. 2009).

As a compromise between sample size and higher spectral resolution, we have undertaken the NEWFIRM medium-band survey (NMBS; van Dokkum et al. 2009; Whitaker et al. 2011) in the COSMOS (Scoville et al. 2007) and AEGIS (Davis et al. 2007) fields. The “high” resolution NIR photometry in combination with the public data available in these fields provides accurate photometric redshifts and stellar population properties out to $z \sim 3$ (Brammer et al. 2009; van Dokkum et al. 2010; Whitaker et al. 2010; Kriek et al. 2010; Marchesini et al.

¹ Harvard-Smithsonian Center for Astrophysics, 60 Garden Street, Cambridge, MA 02138, USA

² Department of Astronomy, Yale University, New Haven, CT 06520, USA

³ Leiden Observatory, Leiden University, NL-2300 RA Leiden, Netherlands

⁴ European Southern Observatory, Alonso de Cordova 3107, Casilla 19001, Vitacura, Santiago, Chile

2010; Wake et al. 2011; Brammer et al. 2011). In the present work we identify groups of analogous galaxies at $0.5 < z < 2.0$ and construct composite SEDs. This approach increases the signal-to-noise and sampling of galaxy SEDs and allows for model-independent stellar population studies. The SEDs are of exquisite quality, showing spectral features, such as the $H\alpha + [N II] + [S II]$ and $H\beta + [O III]$ emission lines, the Balmer or 4000 Å breaks, Mg II absorption at 2800 Å, the continuum break at 2640 Å, and the dust absorption feature at 2175 Å. Thus, these SEDs can be used to study the stellar populations and emission line characteristics of typical galaxies in a very detailed way, which is not possible when the photometry of individual galaxies is considered separately.

This first paper describes our technique, provides an overview of all composite SEDs and example rest-frame optical morphologies, and studies the correlations between the equivalent width (EW) of $H\alpha$, the strength of the 4000 Å break, and the SSFRs of ~ 3500 galaxies at $0.5 < z < 2.0$. Additionally, we compare our measurements to those of low-redshift galaxies from the SDSS and stellar population synthesis (SPS) models, and discuss the implications for the SFHs of galaxies. Other applications of the composite spectra, including the relation between galaxy size and SED type, dust properties, and the demographics of active galactic nuclei (AGNs) will be discussed in future papers.

2. CONSTRUCTING COMPOSITE SEDS

The galaxy sample used to construct the composite SEDs is selected from the NMBS. The NMBS uses five custom NIR filters and covers a total area of 0.4 square degrees in the COSMOS (Scoville et al. 2007) and AEGIS (Davis et al. 2007) fields. The medium-band filter set is combined with publicly available imaging at FUV-to-MIR wavelengths (Erben et al. 2009; Hildebrandt et al. 2009; Barmby et al. 2008; Sanders et al. 2007; Capak et al. 2007) as described in Whitaker et al. (2011). For the work presented in this paper, we limit our sample to the COSMOS field, as medium-band optical photometry from Subaru is available for this field as well (e.g., Taniguchi et al. 2007; Ilbert et al. 2009, Y. Taniguchi et al. in preparation). The high photometric sampling provides accurate photometric redshifts and stellar population properties (e.g., Brammer et al. 2009; van Dokkum et al. 2010; Whitaker et al. 2010). The photometric redshifts and stellar population properties are derived using EAZY (Brammer et al. 2008) and FAST (Kriek et al. 2009a), respectively. In order to limit our sample to high-quality SEDs with rest-frame UV-to-NIR wavelength coverage, we require a redshift of $0.5 < z < 2.0$ and a signal-to-noise (S/N) of 25 in the K -band.

We define 22 artificial rest-frame filters of intermediate bandwidth, evenly spaced in $\log \lambda$ between 1200 Å and 50 000 Å, and compute the fluxes in these filters for all galaxies in our sample, using the method described by Brammer et al. (2009). In Figure 1 we show the filters in comparison to the SEDs of different galaxy types. For each galaxy in our sample we identify analogous galaxies,

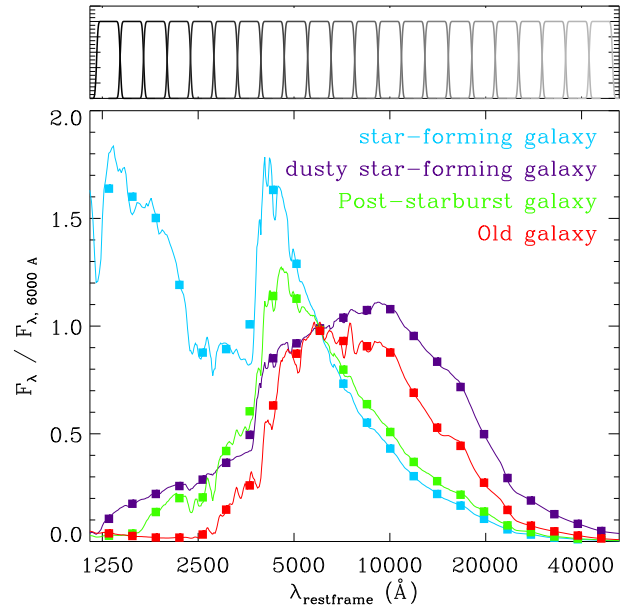


Figure 1. *Top:* The 22 synthetic rest-frame filters used to identify galaxies with similar SED shapes. *Bottom:* SEDs and 22 rest-frame colors for four different galaxy types. This panel illustrates that using these 22 bands we can discriminate between different types and find galaxies with similar SED shapes and thus properties. For example, the value for b between the two closest SEDs in this figure (the dusty star-forming in purple and old galaxy in red) is 0.23.

using the following expression:

$$\sqrt{\frac{\sum (f_{\lambda}^{\text{ob1}} - a_{12} f_{\lambda}^{\text{ob2}})^2}{\sum (f_{\lambda}^{\text{ob1}})^2}} = b_{12} \quad (1)$$

with a the scaling factor

$$a_{12} = \frac{\sum f_{\lambda}^{\text{ob1}} f_{\lambda}^{\text{ob2}}}{\sum (f_{\lambda}^{\text{ob2}})^2} \quad (2)$$

and b the variation between two galaxies. In practice, we generally use fewer than 22 rest-frame filters to relate galaxies, as we only compare the rest-frame wavelength coverage that two galaxies have in common.

We start by taking $b < 0.05$ and identify the galaxy with most analogs; this is the primary galaxy for the first subsample. We choose this value of b as it yields distinct composite SEDs, while keeping the intrinsic scatter per SED type low. By decreasing the value for b we found identical best-fit stellar population models for similar SED types, while for larger values of b the SEDs of individual “analog” galaxies were not well matched.

Next, we remove the primary galaxy and all its analogs from the parent sample and again find the galaxy with the largest number of analogs. We repeat this procedure until the primary galaxy has fewer than 19 analogs. In total we find 32 subsamples with at least 20 galaxies, which include 83% of the total galaxy sample. Some analog galaxies that have been removed in one of the first few iterations might have been a better match with another galaxy type which has been constructed during a later iteration. Thus, after having divided the galaxies into subsamples, we reassign 15% of the galaxies which are a better match with a primary galaxy of another sub-

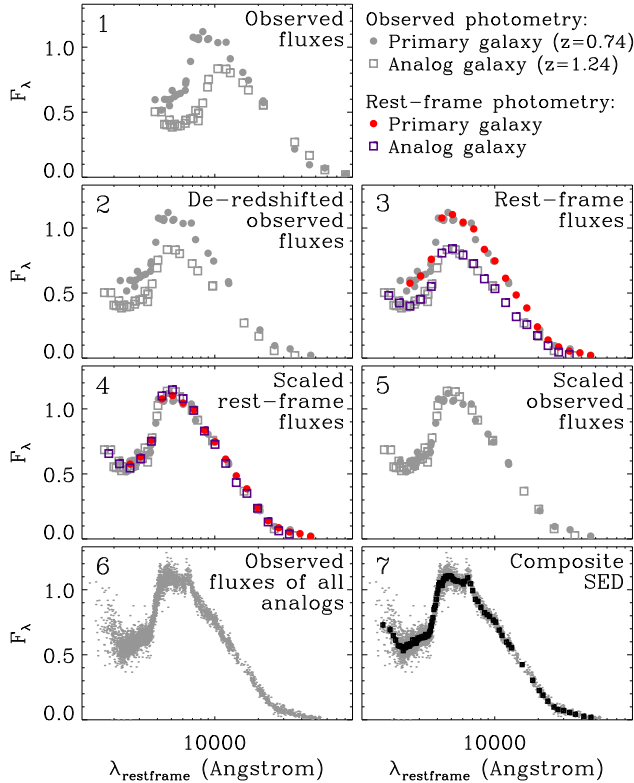


Figure 2. Illustration of our method to construct composite SEDs. In panel 1 we show the primary galaxy and one of its analogs. We de-redshift both galaxies to the rest-frame (panel 2) and determine the fluxes for the artificial filters, as shown in Figure 1 (panel 3). Next, we scale the analog spectrum to its primary using the fluxes of the rest-frame filters they have in common (panel 4). In panel 5 we show the combined scaled and de-redshifted observed photometry of the primary and analog galaxy. We do the same for all analogs, and obtain the combined photometry in panel 6. Finally, we construct a composite SED by averaging the scaled, de-redshifted observed fluxes in wavelength bins.

sample. For example, several galaxies in the subsample of type 3 move to type 2 or 4 (see Section 3).

We create a composite SED for each subsample, by de-redshifting all galaxies, and scaling the observed photometry of the analogs to that of the primary galaxy. Our method is illustrated in Figure 2. Note, that we use *observed* photometry in the stacks, not the 22 rest-frame filters; the 22 filters are only used to find analogs. We construct the composite SEDs by averaging the rest-frame scaled fluxes of the primary and analog galaxies in wavelength bins. The number of data-points per wavelength bin depends on the number of analog galaxies. For each bin we calculate both the error on the mean (using bootstrap resampling) and the scatter in the distribution. To determine the scatter we first derive and remove the running median from all combined photometric data points. Next, we derive the scatter within each bin using the residuals. Finally, we determine the effective filter curve for each bin by adding the de-redshifted, normalized (by total integrated transmission) filter curves of all included data points.

As mentioned above, the composite SEDs include 83% of the total galaxy sample. In Figure 3 we show the parent sample and indicate the 83% that we use in the com-

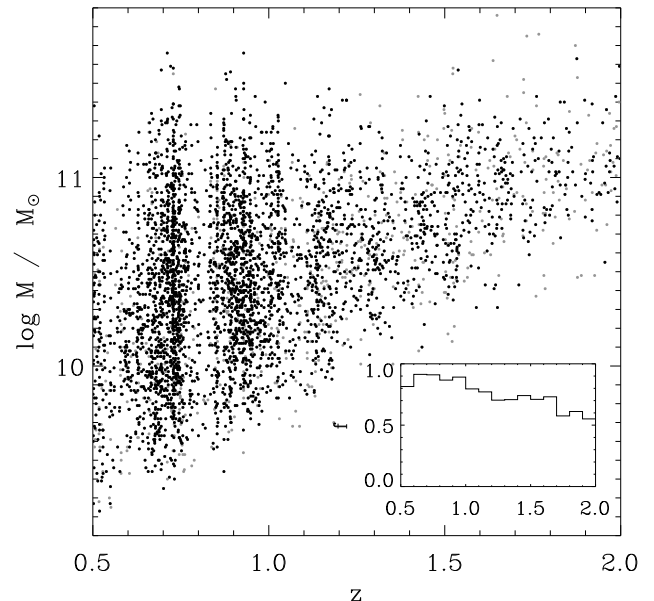


Figure 3. Stellar mass vs. redshift for all 4235 galaxies in the NMBS-COSMOS field with $0.5 < z < 2.0$ and a S/N of > 25 in the K-band. The 83% of the galaxies that are included in the 32 SED types are shown in black, while the remaining 17% are indicated by the gray symbols. In the inset we show the fraction of galaxies that is included as a function of redshift. In Appendix A we further discuss the completeness of our SED sample.

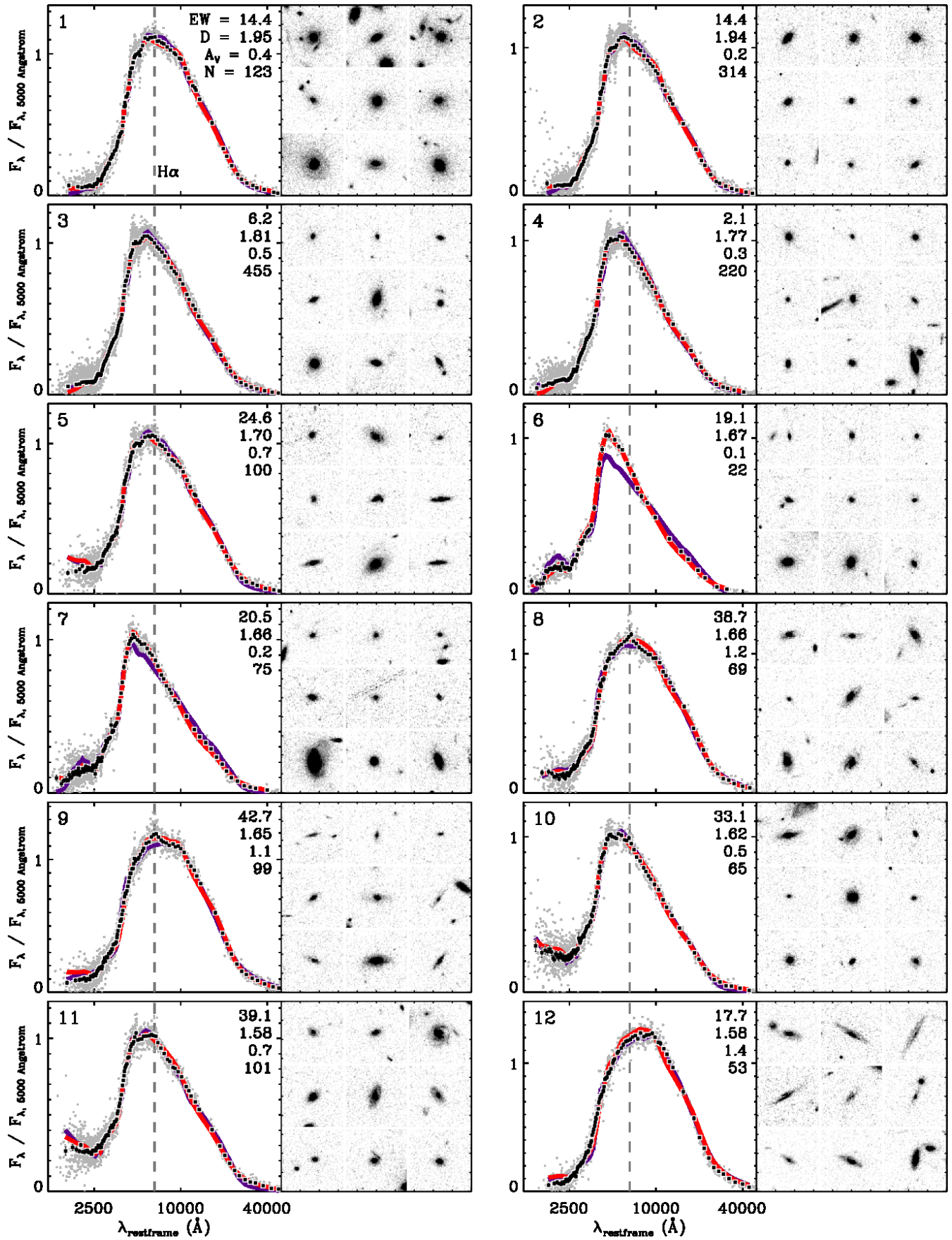
posite SEDs as a function of stellar mass and redshift. The inset shows the completeness fraction as a function of redshift. The figure clearly illustrates that our sample is weighted towards lower redshift, with a median redshift of $z = 0.89$. In Appendix A, we further discuss the completeness of the sample and what types of galaxies we may be missing.

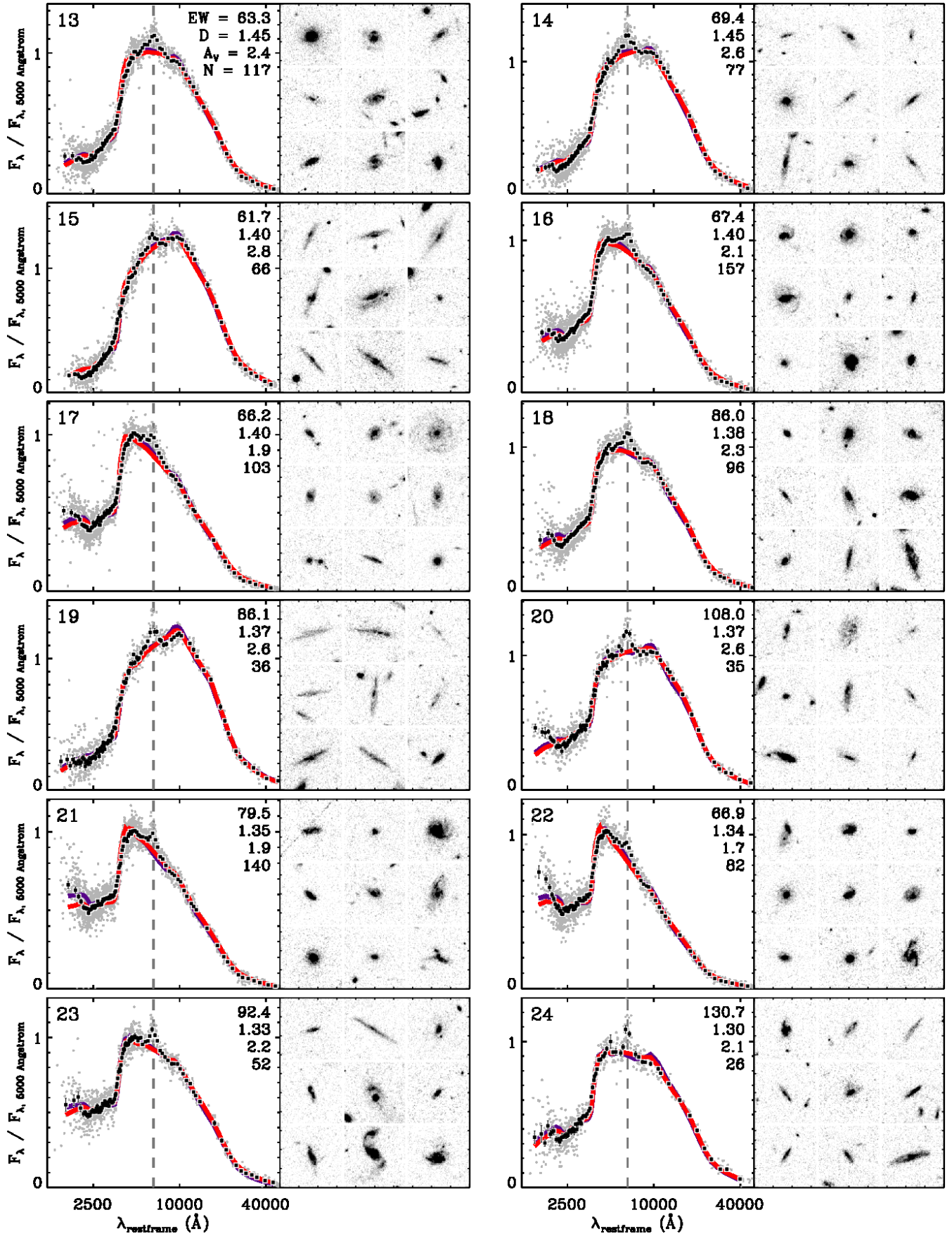
3. ANALYSIS

The composite SEDs are presented in Figure 4. They are of exquisite quality, showing spectral features, such as the H α + [N II]+ [S II] and H β + [O III] emission lines, the Balmer or 4000 \AA breaks, Mg II absorption at 2800 \AA , the continuum break at 2640 \AA , and the dust absorption feature around 2175 \AA . In Figure 5 we indicate all these feature in 3 different SED types: a blue star-forming galaxy type, a dusty star-forming galaxy type, and a quiescent galaxy type. In this section we will study the stellar populations of the different SED types using spectral indices and by comparing the full SED shapes with SPS models.

3.1. SPS fitting

In this section we derive stellar population properties by comparing the composite SEDs with SPS models. We fit the composite SEDs by both the Bruzual & Charlot (2003) and Maraston (2005) SPS models, assuming a delayed exponential SFH of the form $\psi(t) \propto t \exp(-t/\tau)$, and leaving age (t), the e-folding time (τ), the amount of dust attenuation (A_V), and metallicity (Z) as free parameters (see note to Table 2). We assume the Calzetti et al. (2000) attenuation curve, which we implement as a uniform screen. We adopt a Salpeter (1955) initial mass function (IMF). Compared to a Kroupa





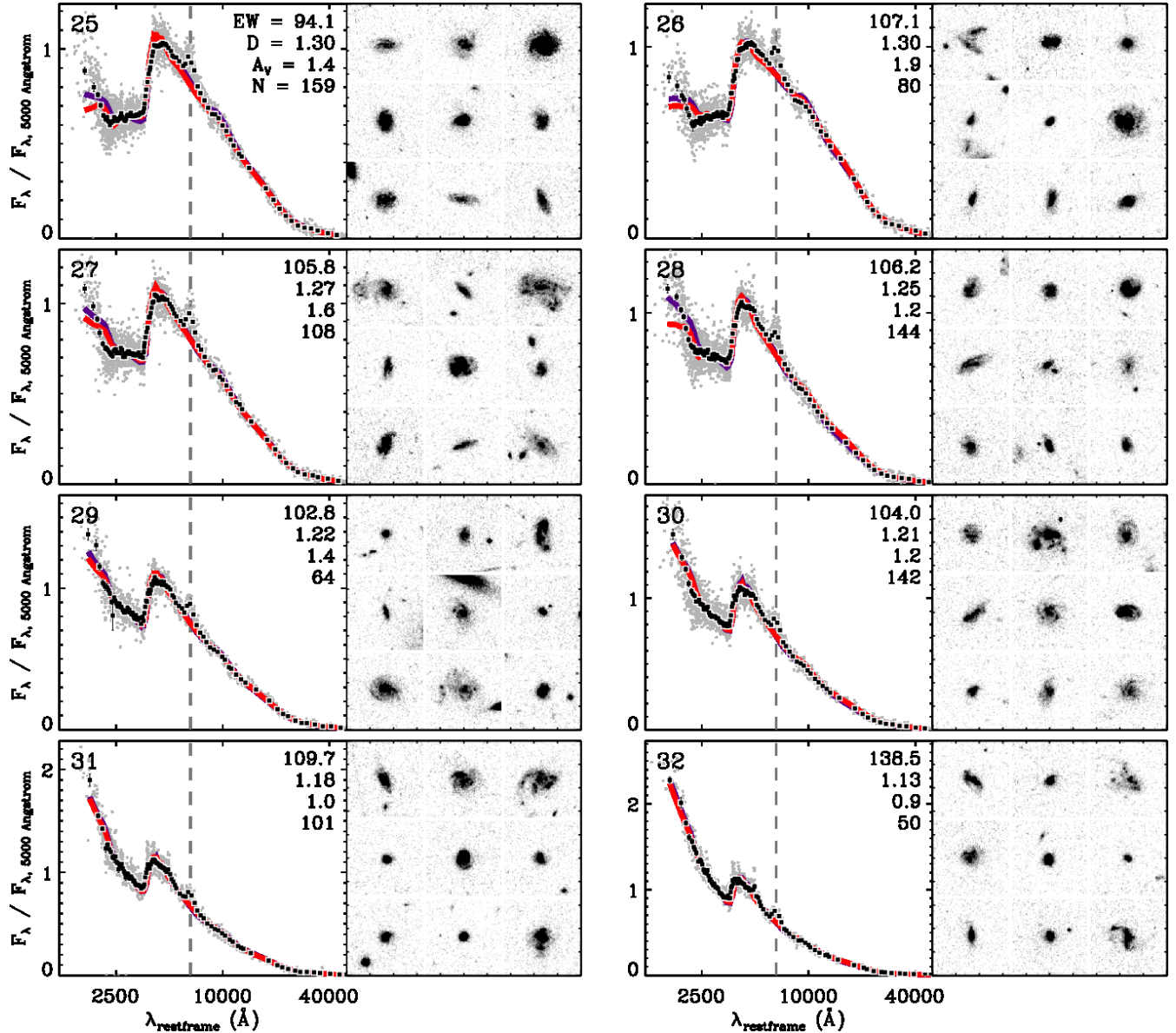


Figure 4. Left panels: Composite SEDs constructed from the NMBS photometry for galaxies at $0.5 < z < 2.0$ with $S/N_K > 25$. The SEDs are ordered according to their $D(4000)$, starting with the SED type with the strongest 4000 \AA break. The dashed line indicates the location of $H\alpha$. The red and purple curves are the best-fit Bruzual & Charlot (2003) and Maraston (2005) models, respectively. The value for $D(4000)$ and $W_{H\alpha+}$, the best-fit value for A_V for the Bruzual & Charlot (2003) models, and the number of galaxy included in the composite SED are printed in each panel. Right panels: For each composite SED we show the i -band HST/ACS images of the nine galaxies closest in redshift to $z = 0.9$, thus probing $\lambda \sim 4000 \text{ \AA}$ in rest-frame.

(2001) or Chabrier (2003) IMF our choice will primarily affect the mass-to-light ratio, and has little impact on other stellar population properties. We mask the bins that are possibly contaminated by $H\alpha$ while fitting. For the photometric uncertainties we take the scatter, and thus our confidence intervals on the stellar population properties essentially reflect the variation within a galaxy subsample.

The best fits for the Bruzual & Charlot (2003) and Maraston (2005) SPS models are represented by the red and purple curves in Figure 4, respectively. The corresponding best-fit values and confidence intervals are given in Table 1. The reduced χ^2 values indicate that most SED types are equally well fit by both

models, though the stellar population properties implied by the fits are not always consistent with each other (see Conroy et al. (2009, 2010a); Conroy & Gunn (2010) for a detailed discussion on the uncertainties in SPS models). The exception though are post-starburst galaxies, which are represented by SED type 6 (and to a lesser extent type 7). As shown in Kriek et al. (2010), the Maraston (2005) models overestimate the contribution of the thermally-pulsing asymptotic giant branch (TP-AGB) stars at NIR wavelengths (see also Conroy & Gunn 2010). SED type 12 is poorly described by both models, though it is not clear why. These galaxies might have been placed at the wrong redshift, resulting in a SED shape which cannot be explained by any

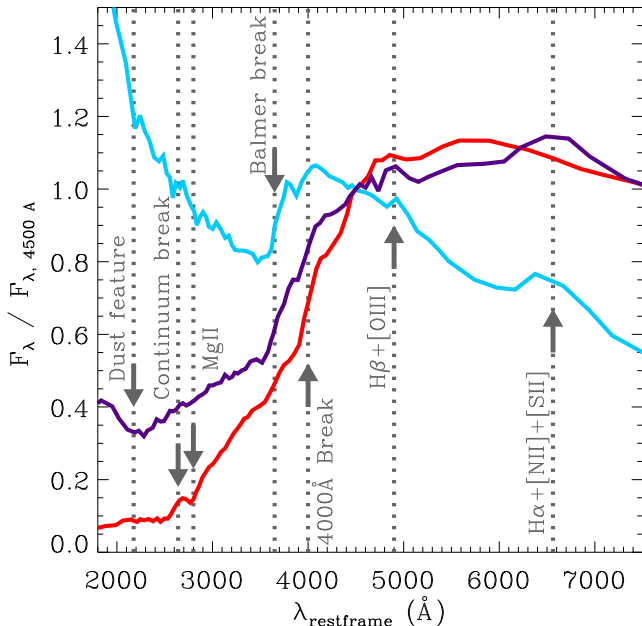


Figure 5. Zoom on the spectroscopic features of three different SED types. For the quiescent type (red) we detect the 4000 Å break, MgII absorption at 2800 Å, and the continuum break at 2640 Å. For the dusty star-forming type (purple) we detect the dust absorption feature at 2175 Å, the H α + [N II]+ [S II] emission line and possibly the H β + [O III] emission line. For the less obscured star-forming type (blue) we detect the Balmer break, and the two sets of blended emission lines.

SPS model. This will be explored in detail in I. Labbé et al. (in preparation).

Many SEDs are poorly fit in the rest-frame UV. This is likely due to the presence of the dust bump at 2175 Å (Stecher 1965), which is not included in the used attenuation model. Although this feature is seen in the Milky Way and several other galaxies (even at high redshift), the exact origin is still unknown (e.g., Draine & Malhotra 1993; Conroy et al. 2010b). We will further investigate this in a future paper.

3.2. $D(4000)$

The composite SEDs allow a direct measurement of the 4000 Å break. The 4000 Å break is due to absorption in the atmospheres of stars and arises because of an accumulation of absorption lines of primarily ionized metals, among which Ca II H and K. As the opacity increases with decreasing stellar temperature, the 4000 Å break gets larger with older ages, and is largest for old and metal-rich stellar populations. The 4000 Å break is generally quantified by $D_n(4000)$ (Balogh et al. 1999), which measures the ratio of the average flux density F_ν in continuum regions blueward (3850-3950 Å) and redward (4000-4100 Å) of the break, or by $D(4000)$ (Bruzual 1983), which uses larger continuum regions around the break (3750-3950 Å and 4050-4250 Å). We measure $D(4000)$ for all our composite SEDs, as it better matches the resolution of our composite SEDs. We determine the confidence intervals using Monte Carlo simulations. For the photometric errors we take the error on the mean, as explained in Section 2.

The break measurements are affected by the low resolution of the medium bands and possible photometric redshifts errors. We correct for the resolution as explained in detail in Appendix C. Summarized, we derive a correction factor for each break measurement using the difference between the break measurement for the original best-fit stellar population model and the best-fit model convolved by the composite filter curves (see Figure in Appendix c). The exact correction factor depends primarily on the strength of the break, but also on the sampling of the composite filters. The original and corrected values for $D(4000)$ are given in Table 1.

Correcting for photometric redshift errors is more challenging, as we do not know the uncertainties for the different SED types. In appendix B we show the effects of the break measurement in case the median random scatter is $\Delta z/(1+z) = 0.005, 0.01, 0.02, \text{ or } 0.04$. We do not apply this correction, but caution that the break measurements, in particular for large values of $D(4000)$, are possibly underestimated.

3.3. H α emission line

Remarkably, we see a bump at the location of H α in most SEDs. In several composite SEDs we also see indications for H β and/or [O III] near 0.5 μm . We measure the equivalent width (EW) of H α + [N II]+ [S II] in the following way. As the best stellar population fits to full SED do not always provide a good fit to the continuum region around H α , we refit the SED restricting the wavelength region to $4000 < \lambda < 10000$ Å, while masking the H α , [N II], [S II], H β , and [O III] emission lines. We subtract the continuum model, thus correcting for the underlying H α absorption. Next, we make an emission-line model, assuming a fixed ratio of the [N II λ 6583]/H α of 0.25, [N II λ 6583]/[N II λ 6548] of 3, and [S II]/H α of 0.3. We convolve the model with the composite filter curves, scale it to fit the data, and derive the total EW of the blended H α , [N II], and [S II] lines.

Confidence intervals on $W_{\text{H}\alpha+}$ are determined using Monte Carlo simulations. We simultaneously vary the photometric uncertainties (following the error on the mean, see Section 2) and the continuum level. For the latter we assume an uncertainty of 1%. We also randomly vary the emission-line ratios in the simulations, assuming an uncertainty of 0.1 on both [N II λ 6583]/H α and [S II]/H α . However, as we derive the total EWs, the line ratios will barely affect the best-fit value or its confidence intervals.

Figure 6 shows examples of the H α emission line for seven composite SEDs, ordered by decreasing $W_{\text{H}\alpha+}$. The consistency between the shape of the observed emission lines and the convolved emission-line models is striking. This result demonstrates the accuracy of our photometric redshifts. In Figure 7 we assess the influence of different values for $\Delta z/(1+z)$ on the shape and strength of the detected H α emission line. The observed shapes give us a rough constraint on the photometric redshift uncertainties for certain SED types. The average random uncertainty is $\Delta z/(1+z) \lesssim 0.02$, consistent with the uncertainties found by Whitaker et al. (2011) when comparing photometric with spectroscopic redshifts. We cannot rule out catastrophic outliers, as they simply would increase the apparent variation among individual SEDs. Thus, the EWs of H α might be slightly underestimated.

Table 2
Stellar population properties, continued

ID	N	IT ^a	Model	Log t yr	Log τ yr	A_V mag	Z	Log SSFR yr ⁻¹	χ^2_{red}	$D(4000)$	$D(4000)_{\text{corr}}$	$W_{\text{H}\alpha+}$ Å
28	144	7	BC03	$8.05^{+0.31}_{-0.05}$	$7.10^{+0.63}_{-0.10}$	$1.20^{+0.30}_{-0.03}$	0.020	$-9.92^{+1.14}_{-0.32}$	0.49	$1.30^{+0.01}_{-0.01}$	$1.25^{+0.07}_{-0.06}$	$106.2^{+11.4}_{-10.5}$
			M05	$8.00^{+0.20}_{-0.10}$	$7.30^{+0.30}_{-0.04}$	$1.30^{+0.10}_{-0.04}$	0.020	$-8.69^{+0.09}_{-0.00}$	0.49			
29	64	28	BC03	$8.20^{+0.06}_{-0.15}$	$7.60^{+0.12}_{-0.20}$	$1.40^{+0.11}_{-0.03}$	0.008	$-8.61^{+0.09}_{-0.00}$	0.54	$1.26^{+0.01}_{-0.01}$	$1.22^{+0.07}_{-0.06}$	$102.8^{+11.5}_{-12.5}$
			M05	$8.15^{+0.05}_{-0.00}$	$7.60^{+0.10}_{-0.01}$	$1.30^{+0.01}_{-0.01}$	0.020	$-8.47^{+0.05}_{-0.00}$	0.61			
30	142	9	BC03	$8.35^{+0.15}_{-0.43}$	$7.80^{+0.20}_{-0.76}$	$1.20^{+0.06}_{-0.12}$	0.008	$-8.65^{+0.04}_{-0.59}$	0.45	$1.24^{+0.01}_{-0.01}$	$1.21^{+0.06}_{-0.06}$	$104.0^{+9.0}_{-9.7}$
			M05	$8.05^{+0.25}_{-0.10}$	$7.40^{+0.39}_{-0.10}$	$1.10^{+0.10}_{-0.04}$	0.020	$-8.60^{+0.10}_{-0.00}$	0.48			
31	101	11	BC03	$8.35^{+0.07}_{-0.18}$	$7.80^{+0.14}_{-0.26}$	$1.00^{+0.12}_{-0.06}$	0.008	$-8.65^{+0.10}_{-0.06}$	0.50	$1.22^{+0.01}_{-0.01}$	$1.18^{+0.06}_{-0.06}$	$109.7^{+12.9}_{-11.6}$
			M05	$8.00^{+0.01}_{-0.05}$	$7.40^{+0.01}_{-0.10}$	$1.00^{+0.01}_{-0.03}$	0.020	$-8.43^{+0.00}_{-0.07}$	0.55			
32	50	21	BC03	$8.30^{+0.26}_{-0.18}$	$7.80^{+0.52}_{-0.25}$	$0.90^{+0.11}_{-0.05}$	0.008	$-8.51^{+0.12}_{-0.04}$	0.55	$1.14^{+0.01}_{-0.01}$	$1.13^{+0.06}_{-0.05}$	$138.5^{+13.5}_{-10.1}$
			M05	$8.00^{+0.28}_{-0.05}$	$7.40^{+0.47}_{-0.03}$	$0.80^{+0.10}_{-0.02}$	0.020	$-8.43^{+0.16}_{-0.00}$	0.63			

Note. — We fit a grid of stellar population models assuming a delayed exponential SFH ($\psi(t) \propto t \exp(-t/\tau)$) with $\log(t/\text{yr})$ between 7.6 and 10.1, in steps of 0.05, $\log(\tau/\text{yr})$ between 7 and 10 in steps of 0.1, and A_V between 0 and 3 in steps of 0.1 mag. We assume the Calzetti et al. (2000) attenuation curve and a Salpeter (1955) IMF. For each model we explore three different metallicities: subsolar (0.01 and 0.008 for the Maraston (2005) and Bruzual & Charlot (2003) models, respectively), solar, and supersolar (0.04 and 0.05 for the Maraston (2005) and Bruzual & Charlot (2003) models, respectively). The errors represent the 68% confidence intervals.

^a The iteration in which the SED is constructed

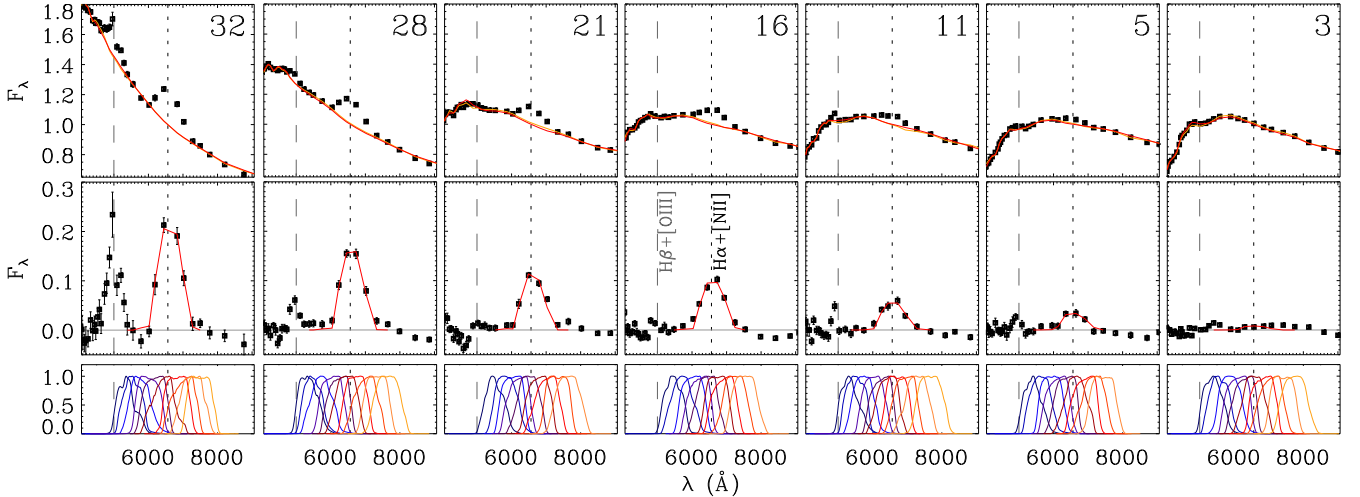


Figure 6. Illustration of H α measurements. The presented composite SEDs cover a wide range in $W_{\text{H}\alpha+}$, and are ordered from the highest to the lowest $W_{\text{H}\alpha+}$ when going from left to right. The continuum emission is fit locally, between 4000-10000 Å, while masking H β , [O III], H α , [N II], and [S II]. The red and orange curves represent the Bruzual & Charlot (2003) and Maraston (2005) continuum models, respectively. In the middle panels we remove the Bruzual & Charlot (2003) continuum model and fit the remaining emission line (red), taking into account the composite filter curves, as represented in the bottom panels. No redshift uncertainties are assumed when fitting the line. The consistency between the observed shapes and those predicted by the filter curves demonstrate the accuracy of our photometric redshifts (see Figure 7). The middle panels also show indications for H β and/or [O III] at \sim 5000 Å in certain cases (dashed lines).

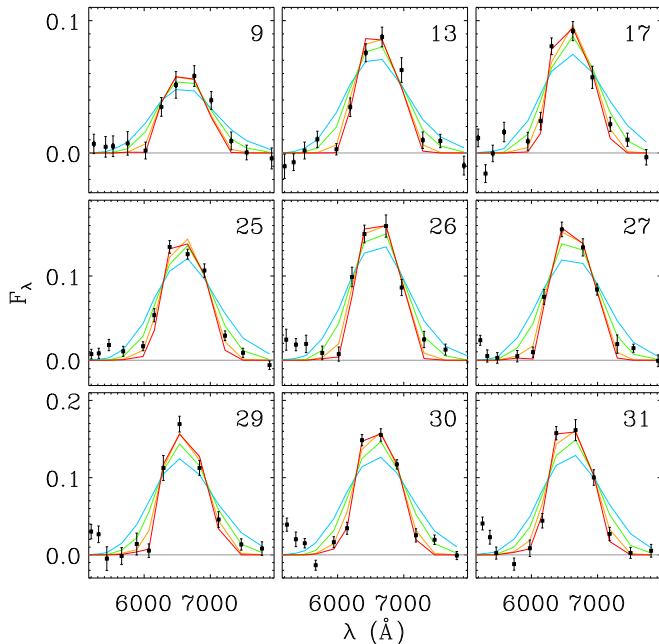


Figure 7. Fits to $H\alpha$ emission lines for different photometric redshift uncertainties. The red curve is the best-fit model when assuming that the photometric redshifts are perfect. For the orange, green, and blue models the random scatter $\Delta z/(1+z)$ is 0.02, 0.04, and 0.06, respectively. This plot illustrates that the NMBS photometric redshifts are certain to $\Delta z/(1+z) \lesssim 0.02$.

3.4. Rest-frame optical morphologies

For each SED type we also show the morphologies of a subsample of the galaxies. We choose the nine galaxies that are closest in redshift to 0.9, as for these galaxies the available HST/ACS i-band imaging from COSMOS probes the rest-frame optical. The images are displayed in Figure 4 next to the composite SEDs. In this paper we will not give a quantitative analysis of the sizes and morphologies; this will be discussed in detail in a future paper.

4. CORRELATIONS

4.1. Star Formation History Indicators

In the previous section we have directly measured two key indicators of present and past star formation in galaxies: $D(4000)$, which is sensitive to the age of the stellar population (as well as metallicity), and $H\alpha$, which measures the instantaneous SFR normalized to the amount of stellar continuum emission at 6563 Å. Together, these parameters measure the star formation history of a galaxy at different times, with $D(4000)$ mostly sensitive to past star formation and $H\alpha$ mostly sensitive to current star formation. Additionally, we derive the SSFR by comparing the full continuum shape with SPS models. The SSFR is the SFR divided by the stellar mass, and thus, similar to $W_{H\alpha+}$, it is a measure of the current versus past star formation, though independently determined.

In Figure 8 we compare the different parameters and show $W_{H\alpha+}$ versus both $D(4000)$ and the SSFR. Note that $D(4000)$ and the modeled SSFRs are not completely independent, as both are derived from the continuum shape, and thus are not directly compared. Remarkably, both panels show a tight correlation. Galaxies with

weak breaks have high values for $W_{H\alpha+}$ and are best fit by stellar population models with high SSFR, while galaxies with low SSFRs and strong 4000 Å breaks have low values for $W_{H\alpha+}$. This is a remarkable result given that the relations are derived without spectroscopy, and are solely based on medium-band photometry. Moreover, the $H\alpha$ emission provides an independent measure of the stellar populations, and confirms our findings based on just the continuum shape. This is a reassuring result, as at the targeted redshift range $H\alpha$ measurements are rare, and thus our understanding of galaxies is primarily based on photometric measurements, which use uncertain stellar population models to interpret the nature of the continuum emission.

There are several caveats. Firstly, as indicated by the solid gray dots and dotted gray lines, the 4000 Å breaks are corrected for resolution (see Section 3.2 and Appendix C). As the correction factors are derived using the best-fit Bruzual & Charlot (2003) models, they may be uncertain for galaxies which are poorly fit. Secondly, none of the values are corrected for photometric redshift uncertainties. Thus, depending on the exact redshift uncertainties, $D(4000)$ and $W_{H\alpha+}$ may have been slightly underestimated for certain SED types. For $D(4000)$ this only affects the SED types with strong breaks. Thirdly, $W_{H\alpha+}$ also includes line contributions from [N II] and [S II]. Their relative contribution will be higher for metal rich systems or for cases in which an AGN is contributing to the line emission. Thus, caution is required when interpreting this plot.

Lastly, although $D(4000)$ is measured over a narrow wavelength interval, dust obscuration slightly affects the break measurement, as indicated by the horizontal dust vector in Figure 8. $W_{H\alpha+}$ is also affected by dust, as the attenuation toward the continuum emission is generally less than the extinction towards star-forming regions (vertical dust vector, Figure 8). In order to illustrate possible offsets, the galaxies in Figure 8 are color coded according to their best-fit values for A_V . As expected, the most dusty galaxies, as indicated in orange, indeed have slightly stronger 4000 Å breaks compared to less obscured galaxies with similar values for $W_{H\alpha+}$. However, we do not correct for this, as the values of A_V are poorly constrained.

4.2. Dust and Morphologies

Taking the measured values for A_V at face value, we find that the oldest galaxies with large $D(4000)$ and low $W_{H\alpha+}$ typically have lower values for A_V than the star-forming galaxies. Interestingly, the four youngest galaxy types with the lowest values for $D(4000)$ and the highest SSFR (29, 30, 31 & 32) have similarly low extinction as galaxies with the strongest breaks. Thus, this may imply that star-forming galaxies are more dusty at intermediate SSFRs.

We also qualitatively investigate how the morphologies change with SED type. When ordering the images by the strength of $D(4000)$, a few simple observations can be made. Firstly, the morphologies of the galaxies with the strongest 4000 Å break are rather regular. This is also found in the local universe and at $z \sim 2.3$ (e.g., van Dokkum et al. 2008). Secondly, more than half of the displayed galaxies of the “oldest” SED type (1) have

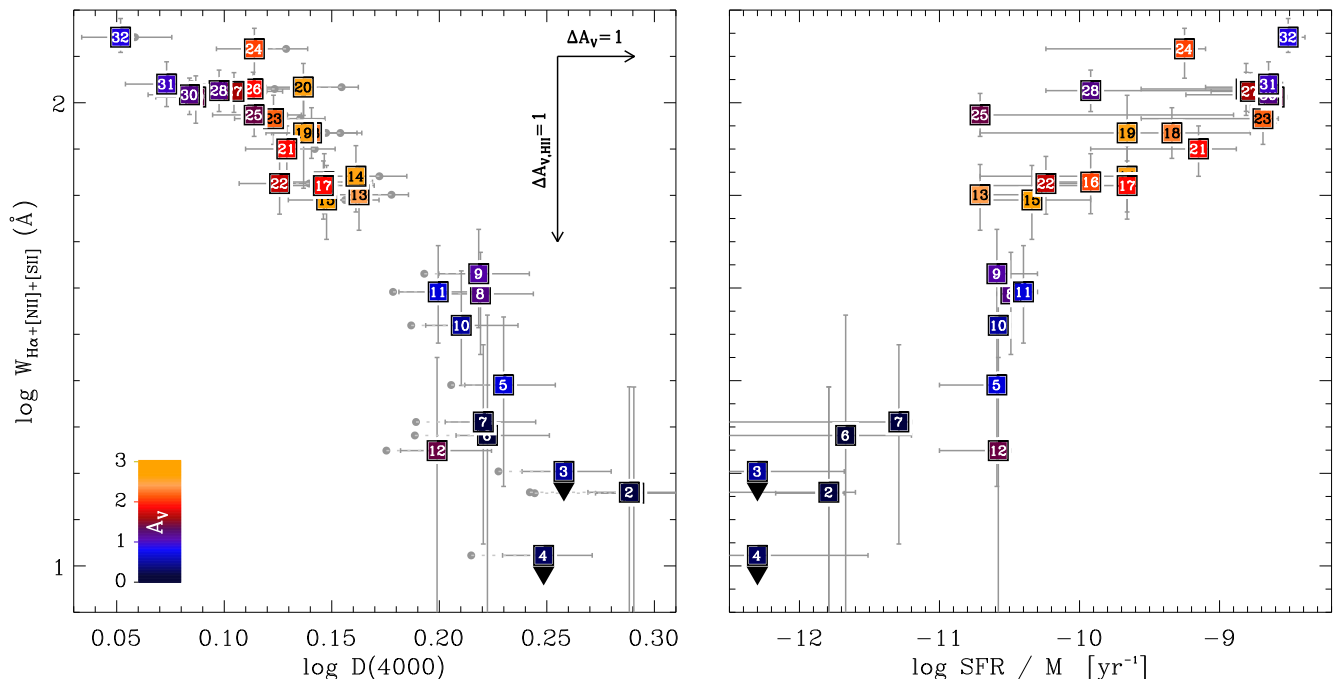


Figure 8. Left: Correlation between $W_{\text{H}\alpha+}$ and $D(4000)$ for the 32 composite SEDs. The corresponding IDs are printed in each symbol. The color coding of the symbols reflect their best-fit value for A_V , as indicated by the color bar in the bottom left. The triangles represent 1σ upper limits. The gray dots represent the values for $D(4000)$ which are uncorrected for the NMBS resolution (see Appendix B). They are connected to the corrected values by the dotted gray lines. The horizontal dust vectors indicates the total attenuation. The vertical dust vector indicates extra extinction towards HII regions. Right: Correlation between $W_{\text{H}\alpha+}$ and the best-fit SSFR. This figure illustrates that $W_{\text{H}\alpha+}$, $D(4000)$, and the best-fit SSFR are strongly correlated: galaxies with shallow breaks have high values for $W_{\text{H}\alpha+}$ and are best fit by stellar population models with high SSFR, while older galaxies with low SSFRs and strong 4000 Å breaks have low values for $W_{\text{H}\alpha+}$.

close neighbors, suggestive of mergers. The sample is small though, and this observation needs to be further assessed. Thirdly, almost all of the displayed galaxies with the highest dust content (e.g., 15 & 19) are edge-on disks. SED types with similar values for $W_{\text{H}\alpha+}$ and $D(4000)$ as the edge-on disks, but with a lower dust content (e.g., 16 & 18) contain several face-on disks, which are likely the same class of objects viewed from a different angle. When going to lower values of $D(4000)$ and higher values of $W_{\text{H}\alpha+}$, more galaxies have irregular and clumpy morphologies. This is consistent with what is found at low (Overzier et al. 2008) or even higher redshift (e.g., Kriek et al. 2009b; Förster Schreiber et al. 2011). A more quantitative analysis will be presented in a future paper.

5. COMPARISON TO LOW-REDSHIFT GALAXIES AND SPS MODEL PREDICTIONS

5.1. Comparison to the Sloan Digital Sky Survey

In this section we compare our measurements with those of low-redshift galaxies from the SDSS (York et al. 2000). For the SDSS galaxies we use the spectroscopic measurements from the MPA-JHU DR7 release (e.g., Kauffmann et al. 2003a; Brinchmann et al. 2004; Tremonti et al. 2004). In Figure 9 we show the $0.5 < z < 2.0$ correlations between $W_{\text{H}\alpha+}$ and $D(4000)$ in comparison to the SDSS galaxies. No similarly derived SSFRs are available for the galaxies in the SDSS and thus they are not shown in the right panel. The sizes of the symbols in Figure 9 reflect the number of galaxies per composite SED.

The relation between $W_{\text{H}\alpha+}$ and $D(4000)$ for the galaxies at $0.5 < z < 2.0$ is similar to the low-redshift SDSS galaxies. There may be a slight offset to higher values of $W_{\text{H}\alpha+}$ for the $z \sim 1$ galaxies. This possible offset is likely not caused by systematic errors. Photometric redshift uncertainties would move the $0.5 < z < 2.0$ relation in the opposite direction, and contamination by an [O II] emission line would make the break at $z \sim 1$ even weaker.

We investigate possible physical explanations by comparing the observations with different model predictions. In Figure 9 we show tracks for different SFHs, which are derived from the Bruzual & Charlot (2003) models in combination with the relation between SFR and H α as given by Kennicutt (1998). The SFHs are visualized in the inset in the right panel in Figure 9. For subsolar, solar, and supersolar metallicity we assume $(\text{N II} + \text{S II})/\text{H}\alpha$ of 0.23, 0.8, and 0.8 respectively (e.g., Denicolo et al. 2002). Comparison with model tracks suggests that galaxies at $z \sim 1$ may have SFHs with longer timescales or higher metallicity compared to $z \sim 0$ galaxies.

The slightly different loci of the SDSS galaxies and our composite SED sample may also be due to systematic differences in the reddening toward HII regions. For example, star-forming regions may be relatively more obscured at low redshift. Higher black-hole accretion rates at earlier times could also explain the offset location of certain SED types at $0.5 < z < 2.0$. This is further supported in the right panel of Figure 9, as the location of several composite SEDs cannot be explained by any SFH. In this context it is interesting to note that in the SDSS many massive, quiescent galaxies are known

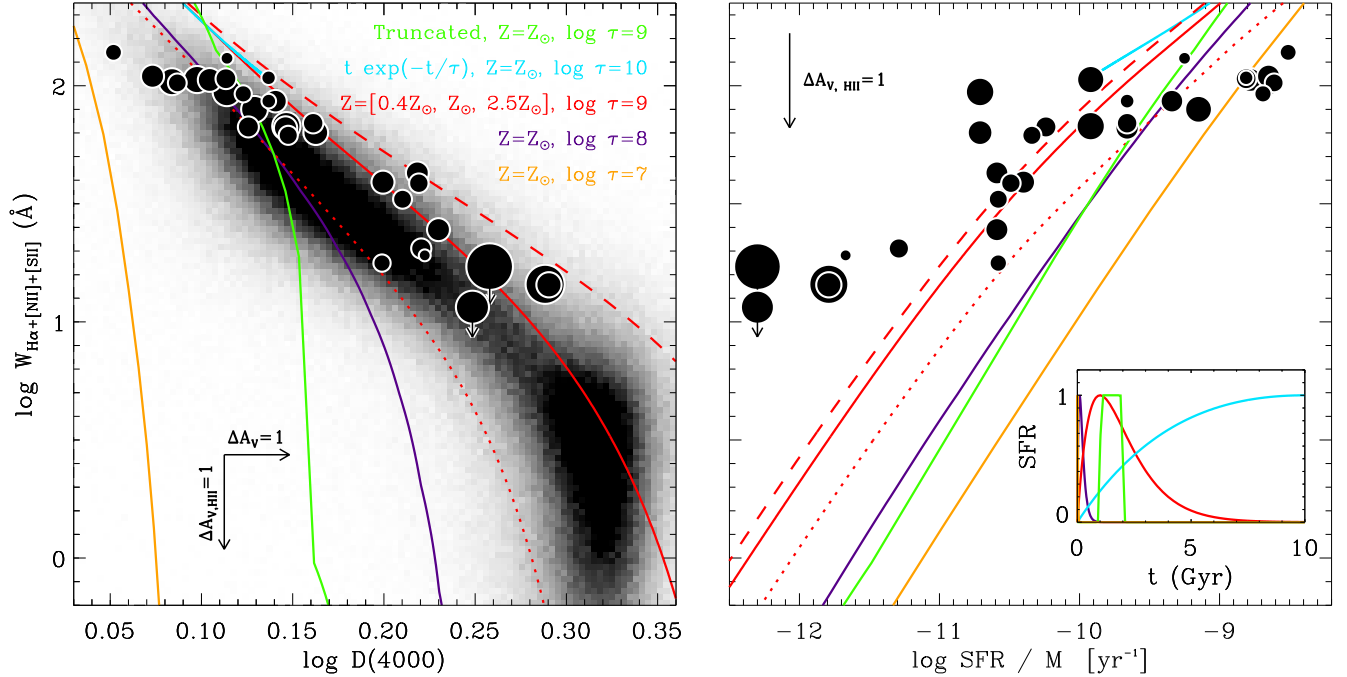


Figure 9. Left: The EW of H α vs the strength of the 4000 Å break for the 32 SED types presented in this work (solid circles) compared to low-redshift galaxies in the SDSS (blocked gray scale) and different SFHs (colored lines). We explore models with SFHs with gradual declining SFRs (red) and contrast those with SFHs with abrupt declines (yellow, green, and purple). The shapes of the SFHs are visualized in the inset in the right panel. Subsolar, solar, and supersolar models are represented by the dotted, solid, and dashed lines, respectively. The sizes of the solid circles scale with the number of galaxies per SED type. For clarity, error-bars are not shown in this figure (see Figure 8). Right: The EW of H α vs. the best-fit modeled specific SFR (assuming the Bruzual & Charlot (2003) models) for the 32 SED types in comparison to different SFHs. Symbols and lines are similar to the left panel. No similarly derived SSFRs are available for the galaxies in the SDSS. Models with abruptly declining SFRs predict that evolved galaxies at low to intermediate $D(4000)$ and SSFRs have low values for $W_{\text{H}\alpha+}$ (yellow, green, and purple). Since the bulk of the galaxies do lie well above those curves, we conclude that these models do not describe the majority of the galaxies. Thus, the suppression of star formation at $z < 2$ is generally a gradual process.

to host LINERs (e.g., Kauffmann et al. 2003b), and thus the $W_{\text{H}\alpha+}$ of the quiescent galaxies in SDSS likely do not reflect their star formation activity. Follow-up spectroscopy is needed to study the nature and origin of the line emission.

5.2. Implication for Star Formation Histories

It is striking that $D(4000)$ and $W_{\text{H}\alpha+}$ correlate so well, given that $W_{\text{H}\alpha+}$ is mostly sensitive to current star formation, while $D(4000)$ primarily reflects the past star formation. As shown by the various model tracks in the left panel of Figure 9, galaxies could in principle occupy roughly all space in between the yellow solid and red dashed line. However, we find that the composite SEDs and the individual SDSS galaxies span a tight relation, close to the solid purple or dotted red line at higher values of $W_{\text{H}\alpha+}$ and close to the red solid line for low values of $W_{\text{H}\alpha+}$. Thus, star-forming galaxies seem better explained by short star formation timescales or lower metallicities, while the more quiescent galaxies are better explained by SFHs with exponential decaying times of about 1 Gyr and solar metallicity.

This finding suggests that the more quiescent galaxies contain stars over a wide age range and that their star formation is gradually declining. To further illustrate this point, we have added a truncated model to Figure 9. This model has a constant SFR for about 1 Gyr, after which the star formation declines to zero. The model is convolved by a Gaussian with a σ of 50 Myr. Thus, the

decline occurs over roughly 0.2 Gyr. This model predicts an abrupt decline of $W_{\text{H}\alpha+}$ compared to the evolution of $D(4000)$, and therefore a population of galaxies with very weak or absent H α emission and weak 4000 Å breaks. However, of all composite SEDs with $D(4000) < 0.24$ all have detected H α emission with a minimum value of 17.7 Å.

We can further quantify this argument by considering the slow suppression model in red and the fast suppression model in green. For each model we derive how long it will take for the 4000 Å break to increase from $\log D(4000) = 0.16$ to $\log D(4000) = 0.24$. For the two models this is 1.56 and 0.78 Gyr, respectively. Thus, if only these two SFHs would exist and both star formation timescales were equally common, we would find that 33% of the galaxies with $\log D(4000) = [0.16, 0.24]$ would have undetected H α emission. However, we find that out of 778 galaxies with $0.16 < \log D(4000) < 0.24$, none have detected H α lower than 17.7 Å. The non-existence of these composite SEDs implies that SFHs with very short star-forming and quenching timescales are quite uncommon. However, short timescales may be possible for the quiescent galaxies that have no detected H α emission (upper limits), if there quenching occurred at $z > 2$.

We note that AGNs may complicate this argument. As we have discussed above, the line emission, in particular for galaxies with strong 4000 Å breaks (both at $z \sim 0$ and $z \sim 1$) may originate from actively-accreting black holes.

Although it is unlikely that the line emission in all these galaxy types is dominated by AGNs, caution is required in the interpretation, and follow-up spectroscopic studies are needed to uncover the origin of the ionized gas.

6. SUMMARY AND CONCLUSIONS

In this paper we study the H α emission line, the 4000 Å break, and the SSFRs of ~ 3500 galaxies at $0.5 < z < 2.0$, using the NMBS high-quality medium-band photometry in the COSMOS field. The optical and NIR medium bands are complemented by UV-to-IR broadband photometry, leading to a total of 33 bands for each galaxy. We have identified analogous galaxies using 22 artificial rest-frame filters which are evenly spaced in $\log \lambda$ between 1200 and 50 000 Å, resulting in 32 galaxy subsamples. Hence, our partitioning method is independent of stellar population models or other assumptions. For each subsample we constructed a composite SED by scaling and de-redshifting the observed photometry.

The composite SEDs are of spectroscopic quality and show spectral features, such as the (blended) H α + [N II]+ [S II] and H β + [O III] emission lines, the Balmer or 4000 Å breaks, Mg II absorption at 2800 Å, the continuum break at 2640 Å, and the dust absorption feature at 2175 Å. Most of these features are not detected in the SEDs of individual galaxies. Thus, the increased S/N and sampling of the composite SEDs enable the detection and measurement of spectral features, which would normally require spectroscopic data. Therefore these SEDs can be used to study the stellar populations and emission line characteristics of typical galaxies in a very detailed way, which is not possible when the photometry of individual galaxies is considered separately. Additionally, the shape and linewidth of the H α emission line yield an independent measure of the photometric redshift errors. Consistent with comparison to spectroscopic redshifts, we find an accuracy of $\Delta z \lesssim 0.02 \times (1 + z)$.

In the present work, we measure $W_{\text{H}\alpha+}$ and $D(4000)$ for all composite SEDs and compare the full SED shapes with SPS models. Most SED types are equally well fit by the Maraston (2005) and Bruzual & Charlot (2003) SPS models. The exception, however, are post-starburst galaxies. As has previously been shown in Kriek et al. (2010), the Maraston (2005) models cannot reproduce the full SED shape of post-starburst galaxies simultaneously. They overpredict the NIR luminosity, implying that these models give too much weight to TP-AGB stars.

We find that $W_{\text{H}\alpha+}$, $D(4000)$ and the best-fit SSFR are all strongly correlated, such that galaxies with shallow breaks have high values for $W_{\text{H}\alpha+}$ and are best fit by stellar population models with high SSFRs. On the other hand, galaxies with strong 4000 Å breaks have low values for $W_{\text{H}\alpha+}$ and are best fit by SPS models with low SSFRs. This is a remarkable result given that the relations are derived without spectroscopy, and solely based on medium-band photometry. Moreover, the H α lines provide an independent measure of the stellar populations and confirm the results based on just the continuum shape. H α measurements at the targeted redshift range are very challenging with spectroscopy, as the line is shifted to NIR wavelengths. At this moment, spectroscopic H α measurements beyond $z = 0.5$

are only available for small or biased galaxy samples (e.g., Shapley et al. 2004; Erb et al. 2006c; Kriek et al. 2008b; Förster Schreiber et al. 2009), and consequently our understanding of galaxies at this epoch is primarily based on photometric measurements, which use uncertain stellar population models to interpret the nature of the continuum emission. The composite SEDs – for the first time – open up the possibility to efficiently study H α emission for large, magnitude-limited galaxy samples, providing a crucial assessment of our photometric studies.

We also study the rest-frame optical morphologies of a subsample of galaxies around $z \sim 1$ for each SED type. Interestingly, we find that with increasing $D(4000)$, galaxies appear to change from irregular and clumpy, to fairly regular disks, to regular early-type systems at the highest $D(4000)$. Strikingly, the most dusty galaxies are typically edge-on disks.

The relation between $W_{\text{H}\alpha+}$ and $D(4000)$ at $0.5 < z < 2.0$ is similar to the low-redshift relation, as determined from the SDSS galaxy sample. There may be a slight offset, such that at fixed value for $D(4000)$, the $W_{\text{H}\alpha+}$ of the $0.5 < z < 2.0$ galaxies is slightly higher than for the low-redshift galaxies. We use simple models to interpret this difference, and show that the rate at which the SFR is declining can explain the difference in $W_{\text{H}\alpha+}$ at fixed $D(4000)$; specifically, the SFRs in $z \sim 1$ galaxies may decline more gradually than at low redshift. The elevated $W_{\text{H}\alpha+}$ may also be explained by higher black hole accretion rates or higher metallicities at earlier times, or by relatively more obscured H II regions at lower redshift.

It is remarkable that $W_{\text{H}\alpha+}$ and $D(4000)$ are so tightly correlated, given that $W_{\text{H}\alpha+}$ is mostly sensitive to current star formation and $D(4000)$ is a measure of the older stellar population, and thus the past star formation. SPS model predictions show that SFHs that decline rapidly after their major burst – such as truncated SFHs or SFHs with short timescales – predict a steeper decline of $W_{\text{H}\alpha+}$ compared to $D(4000)$ than what is observed for the galaxies with intermediate to low values of $W_{\text{H}\alpha+}$. The combination of $D(4000)$ and $W_{\text{H}\alpha+}$ and the best-fit star formation timescales both indicate long star formation timescales of ~ 1 Gyr (for a SFH parametrized by $t \exp(-t/\tau)$) for older galaxy types. This suggests that the suppression of star formation at $z < 2$ is generally not an abrupt, but rather a gradual process. Our finding is consistent with the predictions by high-resolution smoothed particle hydrodynamics (SPH) simulations of massive elliptical galaxies starting from Λ CDM initial conditions (Naab et al. 2007).

The SEDs that we presented here can be used for many additional purposes. For example, we can measure the relative strength of emission lines, the strength of absorption features (e.g., Mg II at 2800 Å), and constrain the dust extinction curve including the 2175 Å dust absorption feature. This paper briefly discussed the morphologies of the different SED types. A more quantitative analysis, with measurements of sizes and ellipticities will be presented in a future paper. For example, by comparing the sizes of galaxies in several evolutionary phases, we can assess theories proposed to explain the size growth of elliptical galaxies (e.g., van Dokkum et al. 2008; Naab et al. 2007, 2009;

Bezanson et al. 2009; Hopkins et al. 2009, 2010). Comparison with other wavelength regimes also offers many interesting possibilities. For instance, X-ray stacks allow the study of AGN demographics among the different types.

Due to the low resolution of the NMBS, it is unfortunately not possible to deblend the emission lines H α , [N II], and [S II] or H β and [O III]. Thus, NIR spectroscopy is needed to test our H α measurements, to derive emission line ratios, and to study the contribution from AGNs to the emission line fluxes. Such measurements would also be very valuable to study the metallicities and Balmer decrements within and among the different samples. Altogether, our composite SEDs in combination with follow-up spectroscopy and other wavelength data enable many different studies to better understand the origin and evolution of galaxies.

We thank the members of the NMBS team for their help with the observations and construction of the catalogs, Charlie Conroy, Ryan Foley, and Jeremiah Ostriker for useful discussions, and the COSMOS and AEGIS teams for the release of high-quality multi-wavelength data sets to the community. M. K. acknowledges support of a Clay Fellowship administered by the Smithsonian Astrophysical Observatory.

REFERENCES

- Baldwin, J., Philips, M., & Terlevich, R. 1981, *PASP*, 93, 5
- Balogh, M.L., Morris, S.L., Yee, H.K.C., Carlberg, R.G., & Ellingson, E. 1999, *ApJ*, 527, 54
- Barnby, P., Huang, J., Ashby, M. L. N., Eisenhardt, P. R. M., Fazio, G. G., Willner, S. P., & Wright, E. L. 2008, *ApJS*, 177, 431
- Bezanson, R., van Dokkum, P. G., Tal, T., Marchesini, D., Kriek, M., Franx, M., & Coppi, P. 2009, *ApJ*, 697, 1290
- Bouwens, R. J., et al. 2011, *ApJ*, 737, 90
- Brammer, G. B., van Dokkum, P. G., & Coppi, P. 2008, *ApJ*, 686, 1503
- Brammer, G. B., et al. 2009, *ApJ*, 706, L173
- Brammer, G. B., et al. 2011, *ApJ*, 739, 24
- Brinchmann, J., Charlot, S., White, S. D. M., Tremonti, C., Kauffmann, G., Heckman, T., & Brinkmann, J. 2004, *MNRAS*, 351, 1151
- Bruzual A.G., 1983, *ApJ*, 273, 105
- Bruzual, G. & Charlot, S. 2003, *MNRAS*, 344, 1000
- Calzetti, D., Armus, L., Bohlin, R. C., Kinney, A. L., Koornheef, J., & Storchi-Bergmann, T. 2000, *ApJ*, 533, 682
- Capak, P., et al. 2007, *ApJS*, 172, 99
- Chabrier, G. 2003, *PASP*, 115, 763
- Conroy, C., Gunn, J. E., & White, M. 2009, *ApJ*, 699, 486
- Conroy, C., White, M., & Gunn, J. E. 2010, *ApJ*, 708, 58
- Conroy, C., & Gunn, J. E. 2010, *ApJ*, 712, 833
- Conroy, C., Schiminovich, D., & Blanton, M. R. 2010, *ApJ*, 718, 184
- Cimatti, A., et al. 2008, *A&A*, 482, 21
- Daddi, E., et al. 2007a, *ApJ*, 670, 156
- Daddi, E., et al. 2007b, *ApJ*, 670, 173
- Damen, M., Förster Schreiber, N. M., Franx, M., Labbé, I., Toft, S., van Dokkum, P. G., & Wuyts, S. 2009, *ApJ*, 690, 937
- Davis, M., et al. 2007, *ApJ*, 660, L1
- Denicolo, G., Terlevich, R., & Terlevich, E. 2002, *MNRAS*, 330, 69
- Draine, B. T., & Malhotra, S. 1993, *ApJ*, 414, 632
- Elbaz, D., et al. 2007, *A&A*, 468, 33
- Erb, D.K., Shapley, A.E., Pettini, M., Steidel, C.C., Reddy, N.A., & Adelberger, K.L. 2006, *ApJ*, 644, 813
- Erb, D.K., Steidel, C.C., Shapley, A.E., Pettini, M., Reddy, N.A., & Adelberger, K.L. 2006, *ApJ*, 646, 107
- Erb, D.K., Steidel, C.C., Shapley, A.E., Pettini, M., Reddy, N.A., & Adelberger, K.L. 2006, *ApJ*, 647, 128
- Erben, T., et al. 2009, *A&A*, 493, 1197
- Förster Schreiber, N. M., et al. 2009, *ApJ*, 706, 1364
- Förster Schreiber, N. M., Shapley, A. E., Erb, D. K., Genzel, R., Steidel, C. C., Bouché, N., Cresci, G., & Davies, R. 2011, *ApJ*, 731, 65
- Franx, M., van Dokkum, P. G., Förster Schreiber, N. M., Wuyts, S., Labbé, I., & Toft, S. 2008, *ApJ*, 688, 770
- Gonzalez, V., Labbé, I., Bouwens, R., Illingworth, G., Franx, M., Kriek, M. & Brammer, G. 2010, *ApJ*, 713, 115
- Hildebrandt, H., Pielorz, J., Erben, T., van Waerbeke, L., Simon, P., & Capak, P. 2009, *A&A*, 498, 725
- Hopkins, P., et al. 2009, *MNRAS*, 398, 898
- Hopkins, P., et al. 2010, *MNRAS*, 401, 1099
- Ilbert, O., et al. 2009, *A&A*, 690, 1236
- Kauffmann, G., et al. 2003a, *MNRAS*, 341, 33
- Kauffmann G., et al. 2003b, *MNRAS*, 346, 1055
- Kewley, L.J., Groves, B., Kauffmann, G., & Heckman, T. 2006, *MNRAS*, 372, 961
- Kennicutt, R.C. 1998, *ARA&A*, 36, 189
- Kriek, M., et al. 2006a, *ApJ*, 645, 44
- Kriek, M., et al. 2006b, *ApJ*, 649, L71
- Kriek, M., et al. 2007, *ApJ*, 669, 776
- Kriek, M., et al. 2008a, *ApJ*, 677, 219
- Kriek, M., van der Wel, A., van Dokkum, P. G., Franx, M., & Illingworth, G. D. 2008b, *ApJ*, 682, 896
- Kriek, M., van Dokkum, P. G., Labbé, I., Franx, M., Illingworth, G. D., Marchesini, D., & Quadri, R. F. 2009a, *ApJ*, 700, 221
- Kriek, M., van Dokkum, P. G., Franx, M., Illingworth, G. D., & Magee, D. K. 2009b, *ApJ*, 705, L71
- Kriek, M., et al. 2010, *ApJ*, 722, L64
- Kroupa, P. 2001, *MNRAS*, 322, 231
- Labbé, I., et al. 2005, *ApJ*, 624, L81
- Labbé, I., et al. 2007, *ApJ*, 665, 944
- Maraston, C. 2005, *MNRAS*, 362, 799
- Maiolino, R., et al. 2008, *A&A*, 488, 463
- Marchesini, D., et al. 2010, *ApJ*, 725, 1277
- McCarthy, P. J., et al. 2004, *ApJ*, 614, L9
- Muzzin, A., Marchesini, D., van Dokkum, P. G., Labbé, I., Kriek, M., & Franx, M. 2009, *ApJ*, 701, 1839
- Muzzin, A., van Dokkum, P., Kriek, M., Labbé, I., Cury, I., Marchesini, D., & Franx, M. 2010, *ApJ*, 725, 742
- Naab, T., Johansson, P. H., Ostriker, J. P., & Efstathiou, G. 2007, *ApJ*, 658, 710
- Naab, T., Johansson, P. H., & Ostriker, J. P. 2009, *ApJ*, 699, L178
- Noeske, K., et al. 2007a, *ApJ*, 660, L43
- Noeske, K., et al. 2007b, *ApJ*, 660, L47
- Oliver, S., et al. 2010, *MNRAS*, 405, 2279
- Overzier, R., et al. 2008, *ApJ*, 677, 37
- Papovich, C., et al. 2007, *ApJ*, 668, 45
- Papovich, C., Finkelstein, S. L., Ferguson, H. C., Lotz, J. M., & Giavalisco, M. 2011, *MNRAS*, in press (arXiv:1007.4554)
- Reddy, N., Erb, D. K., Pettini, M., Steidel, C. C., & Shapley, A. E. 2010, *ApJ*, 712, 1070
- Salim, S., et al. 2007, *ApJ*, 173, 267
- Salpeter, E.E. 1955, *ApJ*, 121, 161
- Sanders, D. B., et al. 2007, *ApJS*, 172, 86
- Scoville, N., et al. 2007, *ApJS*, 172, 1
- Shapley, A. E., Erb, D. K., Pettini, M., Steidel, C. C., & Adelberger, K. L. 2004, *ApJ*, 612, 108
- Stark, D. P., Ellis, R. S., Bunker, A. J., Bundy, K., Targett, T., Benson, A., & Lacy, M. 2009, *ApJ*, 697, 1493
- Stecher, T. P. 1965, *ApJ*, 142, 1683
- Taniguchi, Y., et al. 2007, *ApJS*, 172, 9
- Tremonti, C.A. et al. 2004, *ApJ*, 613, 898
- van Dokkum, P. G., et al. 2006, *ApJ*, 638, L59
- van Dokkum, P. G., et al. 2008, *ApJ*, 677, L5
- van Dokkum, P. G., et al. 2009, *PASP*, 121, 2
- van Dokkum, P. G., et al. 2010, *ApJ*, 709, 1018
- Veilleux, S., & Osterbrock, D. 1987, *ApJS*, 63, 295
- Wake, D. A., et al. 2011, *ApJ*, 728, 46
- Whitaker, K. E., et al. 2010, *ApJ*, 719, 1715
- Whitaker, K. E., et al. 2011, *ApJ*, 735, 86
- Williams, R. J., Quadri, R. F., Franx, M., van Dokkum, P., Labbé, I. 2009, *ApJ*, 691, 1879

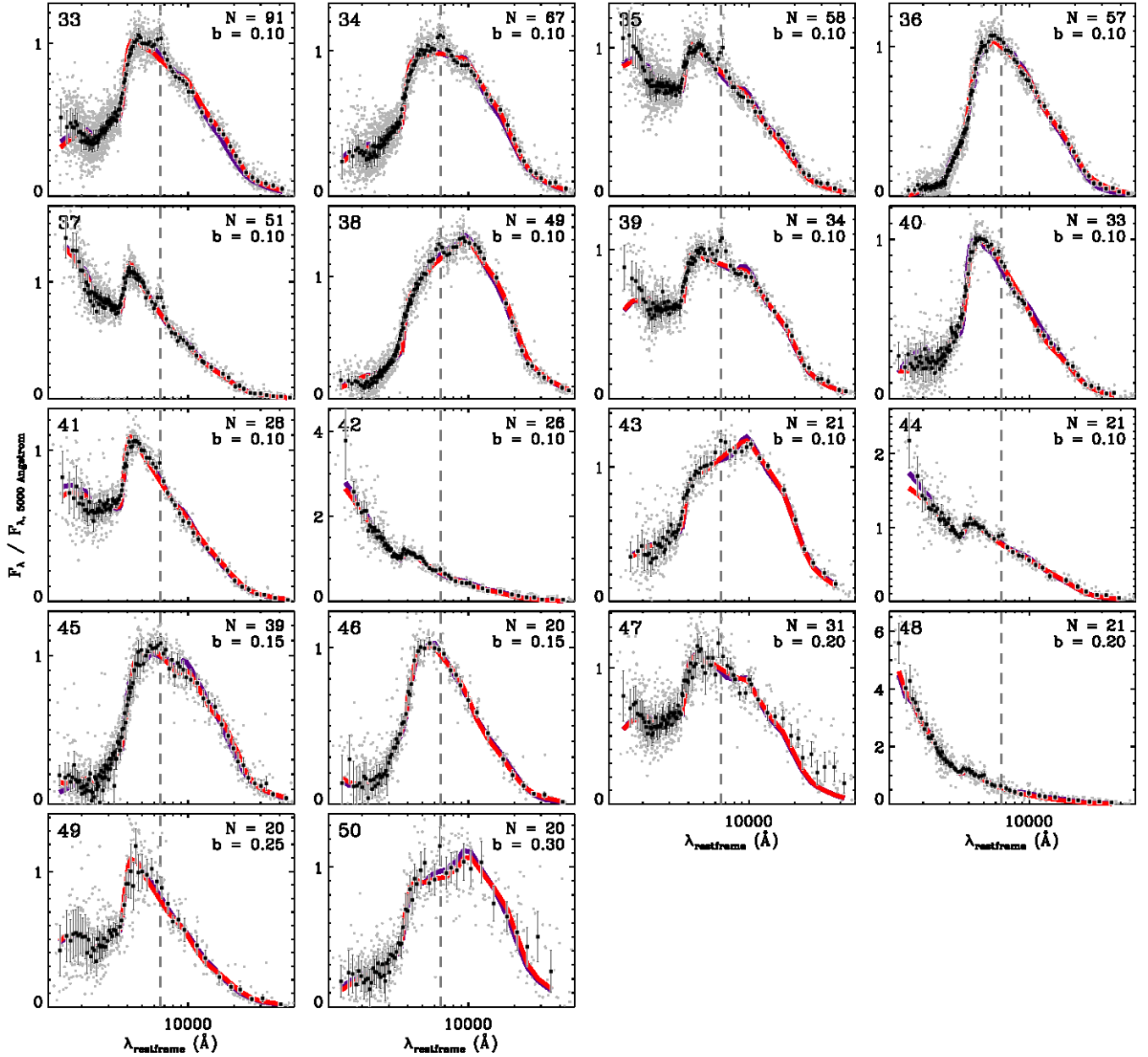


Figure A1. Composite SEDs of the remaining 17% of the parent sample, that were not included in the original 32 galaxy composite SEDs in Figure 4. The symbols and lines are the same as in Figure 4. The remaining galaxies are binned by increasing the value of b in Equation (1), until less than 20 galaxies are left. Most SED types look similar to ones in the initial samples, though with more scatter. However, there are several types which are different, such as SED 42, 44 and 48. Thus, the most un-obscured star-forming galaxies are likely missed in our primary sample.

York, D. G. et al. 2000, AJ, 120, 1579

APPENDIX

APPENDIX A: COMPLETENESS

The composite SED collection of 32 template constitutes 83% of the ~ 4200 galaxies in our parent sample. Here, we assess the completeness and discuss which SED types we are possibly missing. For the 17% of the remaining galaxies we use the same technique to find analogous galaxies, but now taking $b = 0.1$ in Equation (1). We divide up the sample, such that each primary has at least 19 analog galaxies and construct 12 composite SEDs with this value of b . They are presented in Figure A1 (33-44). Next we increase b to 0.15, 0.20, 0.25 and 0.30 until the remaining sample is less than 20 galaxies. The six composite SEDs constructed with values of $b > 0.1$ are shown in Figure A1 as well.

Many SED types in Figure A1 look similar to one of the 32 galaxy types in the main sample. However, SEDs 42, 44 and 48 are not represented in the 32 galaxy types. Thus, the most un-obscured star-forming galaxies are likely missed

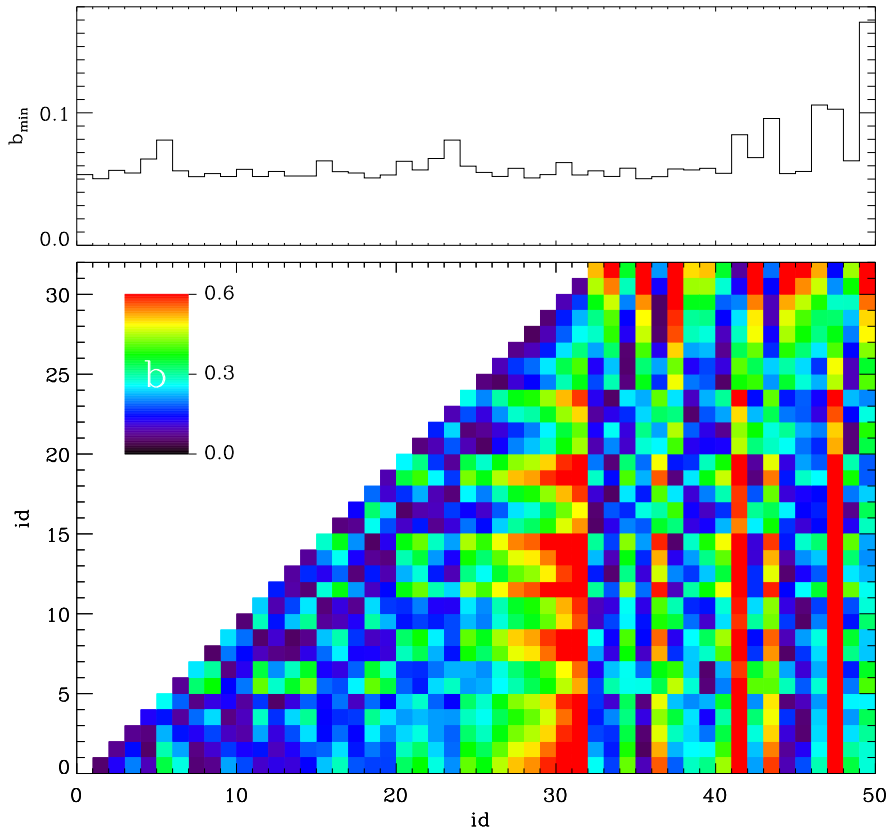


Figure A2. Bottom: The value of the correlation quantity b (see Equation 1) between the primary galaxies of the different subsamples. Top: the minimum value of b for the primary galaxy of a certain SED types, when compared to all other primaries in the main sample (first 32 SEDs).

in our primary sample. Their SSFRs are in the order of $\log \text{SSFR} = [-7, -8]$. However, as their Balmer breaks are very shallow and as their Lyman breaks are not in the observed window for $0.5 < z < 2.0$, their photometric redshifts have large uncertainties. Thus, the measured $W_{\text{H}\alpha+}$ for these galaxies is highly uncertain. Galaxy types with high values for b give less insight into the remaining galaxy population, as they are likely composed of intrinsically different SED types.

To do a more quantitative analysis, we relate all primary galaxies with the primaries of the main sample in Figure A2. In the bottom panel we indicate the values for b (see Equation 1) between the different SED types. In the top panel we show the minimum value of b for each SED type, when compared to all other primary galaxies of the main sample. This figure illustrates that our main sample is well sampled, with typical b values of ~ 0.05 - 0.06 between the closest types. SED types 6 and 24 have slightly higher values with $b \sim 0.08$. The SED types in the $b = 0.1$ sample (SED type 33-44, Figure A1) relate to the main sample with values of $b \sim 0.06$. The exceptions are SED types 42 and 44. As mentioned above, these galaxies are indeed not represented in our main sample. The SED types with higher values of b are less correlated to the primaries of the main samples. For some types (e.g., 48) this means that their SED is very different from the main sample, while for other types this may reflect the fact that the large variation of galaxies within one type leads to unphysical composite SEDs.

APPENDIX B: STACKING TEST

In this appendix we assess whether our stacking technique indeed yields the average properties of the individual galaxies in the subsamples. We do so by applying our stacking technique to galaxy spectra in the SDSS. We start with 10 000 galaxy spectra in the SDSS and select all galaxies at $0.095 < z < 1.05$. For each galaxy we determine the fluxes in the rest-frame filters (shown in Figure 1), which overlap with the spectra. Next, we correlate all galaxies with each other using Equation 1. As the galaxies are matched using only three filters, we start with a smaller value for b of 0.01 to find analogs. Similar as for the higher redshift sample, we increase the value for b , requiring that each SED type consists of a minimum of 20 galaxies. We increase b until nearly all galaxies are part of an SED bin. In total we have 26 subsamples for which we construct the composite SEDs.

We measure $D(4000)$ in the composite spectra and compare these to the mean of the individual measurements in Figure B1. The individual measurements are adopted from the MPA-JHU DR7 catalogs. The color of the datapoints reflect the value of b , and thus the scatter of the properties within the subsamples. The errorbars on the mean properties of the individual galaxies are derived using bootstrapping. We also calculate the errors on the stacked

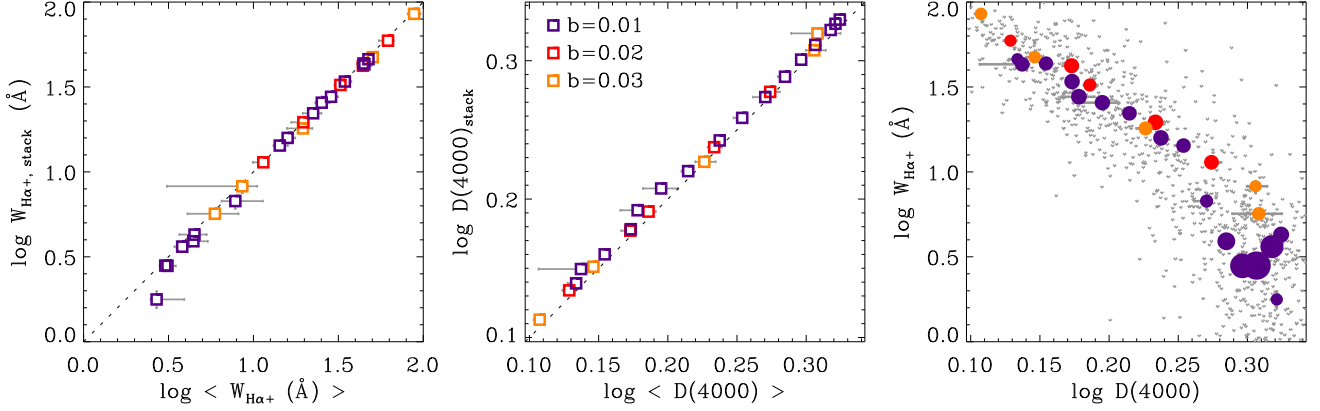


Figure B1. Comparison of the average values of individual galaxies with the value as measured from the stacked spectrum of the same individual galaxies, for both $W_{\text{H}\alpha^+}$ (left) and $D(4000)$ (middle). For this test we use ~ 1000 galaxies in SDSS at $z \sim 0.1$, and construct the stacked spectra in the same way as for the higher redshift sample. The right panel shows $W_{\text{H}\alpha^+}$ vs. $D(4000)$, with the individual measurements represented by the small gray dots and the stacked values represented by the solid circles. The sizes of the solid circles scale with the number of galaxies in the stack. The colors of the symbols indicate the value for b (see Equation 1) of the stacked spectrum. This figure illustrates that with our stacking method we recover the average properties of the individual galaxies.

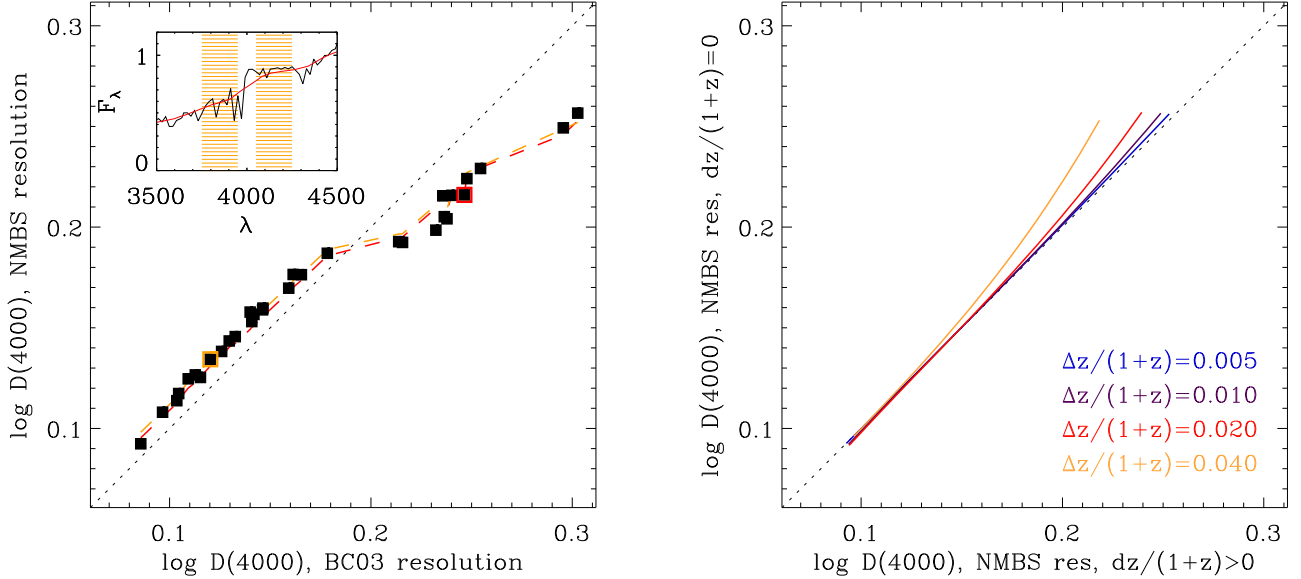


Figure C1. Left: Measurements for $D(4000)$ derived from the best-fit Bruzual & Charlot (2003) models to the composite SED at the original resolution versus $D(4000)$ measured after convolving the best-fit model with the composite filter curves. For each composite SED we derive a resolution correction factor based on the ratio of these two $D(4000)$ measurements. The correction factor depends on the strength of the break and the composite filter curves. The dashed lines represent the correlations for two particular filter sets. Right: The effect of photometric redshift errors on the break measurement. We do not correct for this effect, as the exact redshift uncertainties for each SED type are unknown. Nonetheless, with this exercise we caution that the measurements for $D(4000)$ for larger breaks may be underestimated.

values using simulated spectra, which are constructed using the noise spectra.

There is good agreement between the break measurements for $D(4000)$ for the stack and the individual systems, with a small systematic offset toward higher values for the stack. The different measurements for $W_{\text{H}\alpha^+}$ are also in very good agreement, except for at the lowest value of $W_{\text{H}\alpha^+}$ of 2-3 Å. This is reassuring, in particular given the fact that both measurements use different techniques to correct for the underlying Balmer absorption. The agreement does not worsen for larger values of b ; even for composite spectra which are constructed from galaxies which exhibit a large intrinsic scatter in SEDs, the stacks still recover the average of the individual measurements.

APPENDIX C: $D(4000)$ CORRECTION

The composite SEDs allow the direct measurement of the 4000 Å break. In this paper we use the index $D(4000)$ by Bruzual (1983) to quantify its strength. This index measures the difference in flux in small wavelength regions bracketing the break, as indicated by the orange shaded areas in the inset in Figure C1. However, this measurement

will be affected by the low resolution of the composite SED. The inset in Figure C1 shows a synthetic SED in the region around the break. The red curve shows this same SED, but now convolved by the composite filter curves. This figure clearly illustrates that for this case the convolved SED will yield a slightly lower value for $D(4000)$ than the actual SED.

We can correct for this effect as we know the composite filter curves for all SEDs. For each SED type we derive a correction factor using its best-fit stellar population model. First, we measure the break in the original best fit, and then we derive $D(4000)$ for the same model, but now convolved with the composite filter curves. We show both these measurements for each SED type in Figure C1. We obtain the correction factor by dividing them by each other, and we assume a 5% error on this factor.

The correction factor is dependent on the actual value of $D(4000)$ and the sampling of the composite filter curves. For example, Figure C1 shows that for small breaks the correction factors are close to unity. This is not surprising, as for these galaxies $D(4000)$ measures the slope of the continuum, and this is less affected by resolution. However, the larger the break, the larger the correction factor. The dependence on the filter curves is illustrated using the dashed colored lines. These lines indicate the correction for different values of $D(4000)$ for a particular composite filter set. For SEDs with less composite filters the corrections are larger. Note that the break measurement is not always consistent with that of the best-fit model, and thus the distribution of $D(4000)$ in Figure C1 is slightly different from the measured distribution.

The break measurements are also affected by photometric redshift uncertainties. In the right panel in Figure C1 we show the effects on the break measurements for different values of $\Delta z/(1+z)$. The widths of the blended H α emission lines (see Figure 7) indicate a photometric redshift uncertainty of $\Delta z/(1+z) < 0.02$. Comparison with spectroscopic redshifts shows that the photometric redshifts in the NMBS have an uncertainty of $\Delta z/(1+z) = 0.01 - 0.02$ (Whitaker et al. 2011). However, the uncertainties will depend on SED type (e.g., Kriek et al. 2008a), and as the exact scatter per SED type is unknown, we have decided not to correct the break measurements for photometric redshift uncertainties. This means that the values for $D(4000)$, in particular for galaxies with strong breaks may be underestimated.